Predictive Haemodynamics in a One-Dimensional Human Carotid Artery Bifurcation. Part I: Application to Stent Design

Vijaya B. Kolachalama, Neil W. Bressloff*, Prasanth B. Nair, and Clifford P. Shearman

Abstract—**A diagnostic technique is proposed to identify patients with carotid stenosis who could most benefit from angioplasty followed by stent implantation. This methodology involves performing a parametric study to investigate the haemodynamic behavior due to alterations in the stenosis shapes in the internal carotid artery (ICA). A pulsatile 1-D Navier-Stokes solver incorporating fluid-wall interactions for a Newtonian fluid which predicts pressure and flow in the human carotid artery bifurcation is used for the numerical simulations. In order to assess the performance of each individual geometry, we introduce pressure variation factor as a metric to directly compare the global effect of variations in the geometry. It is shown that the probability of an overall catastrophic effect is higher when the stenosis is present in the upstream segment of the ICA. Furthermore, maximum pressure is used to quantify the local effects of geometry changes. The location of the peak and extent of stenosis are found not to influence maximum pressure. We also show how these metrics respond after stent deployment into the stenosed part of the ICA. In particular, it is found that localized pressure peaks do not depend on the length of a stent. Finally, we demonstrate how these metrics may be applied to cost-effectively predict the benefit of stenting.**

Index Terms—**Carotid artery, diagnostic techniques, parametric study, stent design, 1–D blood flow.**

I. Introduction

In recent years, significant impetus has been given towards the use of simplified models for understanding haemodynamics of the cardiovascular system [1]–[4]. Research using these models has been inclined towards improving patient specific diagnosis and treatment, surgical planning [3] and enhanced design of artificial organs and stents. These simplified mathematical and numerical models provide a reasonable understanding of the disease at an economic computational cost without compromising significantly on accuracy. Furthermore, 1-D blood flow simulations in compliant vessels can help us to study the effects of disease of an artery on flow and wave propagation patterns [4]. Diseased arteries are increasingly being treated using interventional procedures such as balloon angioplasty which involves dilation of the narrowed segment followed by insertion of a stent (a lattice-shaped expandable metallic tube as shown in Fig. 1). The stent acts as an expanding scaffold and remains in place permanently. Due to the presence of this foreign body, which is far more rigid than the arterial tissue, the material properties change abruptly and this may lead to alterations in pressure and flow patterns [5]. Re-stenosis is a common problem occurring within six months after stent implantation and has been observed through follow-up procedures on many patients [6], [7]. Re-stenosis is characterized by smooth muscle cells migration and proliferation and by endothelial cell proliferation. It often occurs at the interface between the graft and native vessel or at points of mechanical stress. Localized pressure peaks can be generated by the cardiac pulse and the superposition of waves reflected by the stent. Notwithstanding the impact of bio-chemical effects, 1-D flow models have been developed to understand the effects of changes in geometry and in the material properties of the blood vessel wall on the associated pressure patterns [4]. These studies were performed on idealized models and hence conclusions derived from them may be limited due to inter/intra individual differences in the geometry and the

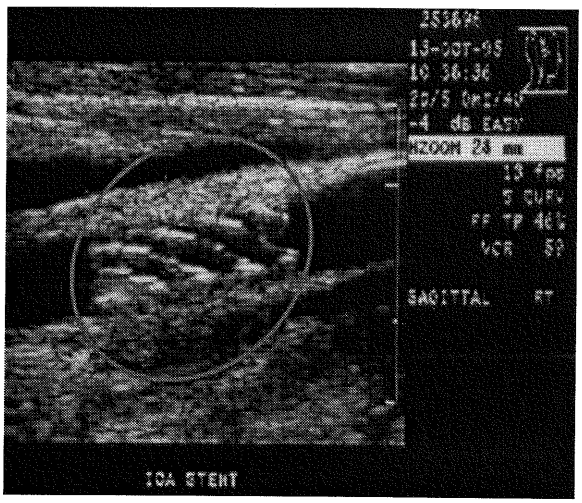

Fig. 1. Duplex ultrasound scan illustrating stent deployment in the ICA. The highlighted region shows the lattice shaped structure of the stent.

Manuscript received May 9, 2006; revised September 24, 2006. *Asterisk indicates correpsonding author.*

V. B. Kolachalama is with the Biomedical Engineering Center, Harvard-MIT Division of Health Sciences and Technology, Cambridge, MA, 02139 USA (e-mail: vbk@mit.edu).

*N. W. Bressloff is with the Computational Engineering and Design Centre, School of Engineering Sciences, University of Southampton, SO17 1BJ, U.K. (e-mail: nwb@soton.ac.uk).

P. B. Nair is with the Computational Engineering and Design Centre, School of Engineering Sciences, University of Southampton, SO17 1BJ, U.K. (e-mail: pbn@soton.ac.uk).

C. P. Shearman is with the Department of Vascular Surgery, Southampton General Hospital, SO16 6YD, U.K. (e-mail: c.p.shearman@soton.ac.uk).

Color versions of one or more of the figures in this paper are available online at http://ieeexplore.ieee.org.

Digital Object Identifier 10.1109/TBME.2006.889188

mechanical properties. It is likely that a parametric study would be beneficial to understand the impact of these differences on the appearance and progression of the disease. We hypothesize that this methodology may allow optimisation of stent design to limit vascular injury and perhaps inhibit re-stenosis. These sort of approaches may also provide guidelines on the suitability of interventional options and in particular to identify patients on whom angioplasty followed by stenting may be favorable.

In this paper, a 1-D deterministic numerical model which can predict flow and pressure in a systemic elastic arterial bifurcation using a pulsatile 1-D Navier-Stokes solver for a Newtonian fluid is used [2], [8]. We selected the human carotid artery bifurcation as the anatomical site for analysis as it is a common site for arterial disease to occur. A metric, pressure variation factor (PVF) is defined and a parametric analysis is conducted to understand how this metric behaves with respect to the parameters defining the stenosis in the internal carotid artery (ICA). Throughout this study, we refer to stenosis as the percentage of area reduction in a vessel and for simplicity, area stenosis and stenosis will be used interchangeably. We then insert a stent near the stenosed region in the ICA and show how PVF varies due to variations in the length of the stent and its Young's modulus. Similar results are also presented by considering maximum pressure (p_m^*) as the metric.

The next section discusses the theoretical and numerical aspects of the 1-D flow solver including the geometry and elasticity of the vessel, the system of equations governing the flow, the numerical technique used to solve the flow followed by a discussion on the boundary conditions. Finally, key results are presented and discussed.

II. Preliminaries

A. Geometry and Elasticity of the Vessel

An individual large systemic artery has a geometry which generally tapers along its length. The radius of the vessel follows an exponential curve of the form

$$r(x) = r_u \exp(kx) \tag{1}$$

where r_u (Units - cm) denotes the mean upstream cross-section of the vessel, k (Units - cm^{-1}) signifies the tapering factor and the length, x (Units - cm), varies between 0 and L, where L (Units - cm) is the length of a vessel. The upstream cross-section of the artery is greater than the downstream cross-section and they are related to each other according to the tapering factor

$$k = \log(r_d/r_u)/L \tag{2}$$

where r_d (Units - cm) denotes the downstream cross-section of the vessel. (The effect of variation in the value of k can be seen in Fig. 6). From the above equations, the radius of the vessel becomes

$$r_o(x) = r_u(r_d/r_u)^{x/L} \tag{3}$$

where $r_o(x)$ (Units - cm) is the radius of the vessel at zero transmural pressure ($p = p_o$) (Units - mm.Hg). The elastic properties of the vessel can be estimated from the Young's modulus, E (Units - $\mathrm{g.cm}^{-1}.\mathrm{s}^{-2}$), the wall thickness, h (Units - cm), and the radius of the vessel, r_o. An empirically estimated relation between them was proposed in [8] which is as follows:

$$Eh/r_o = k_1 \exp(k_2 r_o) + k_3. \tag{4}$$

The empirical estimates of the constants k_1, k_2 and k_3 are taken as 2×10^7 $\mathrm{g.cm}^{-1}.\mathrm{s}^{-2}$, -22.53 cm^{-1} and 8.65×10^5 $\mathrm{g.cm}^{-1}.\mathrm{s}^{-2}$ respectively.

B. Governing Equations

The complete derivation of the governing equations can be found in [2], [8]. However, we outline some details for completeness. The total system of continuity and momentum equations can be written in conservation form as

$$\frac{\partial}{\partial t}\begin{pmatrix} A \\ q \end{pmatrix} + \frac{\partial}{\partial x}\begin{pmatrix} q \\ \frac{q^2}{A} + \frac{f}{\rho}\sqrt{A_o A} \end{pmatrix} = \begin{pmatrix} 0 \\ -\frac{2\pi\nu r q}{\delta A} + \frac{1}{\rho}\left(2\sqrt{A}\left(\sqrt{\pi}f + \sqrt{A_o}\frac{df}{dr_o}\right) - A\frac{df}{dr_o}\right)\frac{dr_o}{dx} \end{pmatrix} \tag{5}$$

where A (Units - cm^2) is the cross-sectional area, q is the flow (Units - $\mathrm{cm}^3.\mathrm{s}^{-1}$), $f(r_o) = 4Eh/3r_o$ (Units - $\mathrm{g.cm}^{-1}.\mathrm{s}^{-2}$), A_o (Units - cm^2) is the cross-sectional area at zero transmural pressure, ν (Units - $\mathrm{cm}^2.\mathrm{s}^{-1}$) is the kinematic viscosity, δ (Units - cm) is the boundary layer thickness, ρ (Units - $\mathrm{g.cm}^{-3}$) is the density of blood and

$$\frac{df}{dr_o} = \frac{4}{3}k_1 k_2 \exp(k_2 r_o) \tag{6}$$

with units of $\mathrm{g.cm}^{-2}.\mathrm{s}^{-2}$. An axi-symmetric flow without swirl is assumed to derive these governing equations. In this derivation, only the radial viscous term is used and the longitudinal viscous term is neglected because the ratio between the length of a blood vessel with its radius is assumed to be very large. The thickness of the boundary layer is estimated as

$$\delta = \sqrt{\nu T/(2\pi)} \tag{7}$$

where T (Units - sec) is the time period of one cycle. Also, the Reynolds number is found using the characteristic parameters as

$$\Re = q_c/(\nu r_c). \tag{8}$$

We assume a laminar flow in these tapered vessels and since the flow is time dependent, the velocity profile is rather flat except for a thin boundary layer of width δ (Units - cm) in which the

transition to zero velocity at the wall is made. Using (4), the pressure (Units - mm.Hg) is related in the state equation as

$$p(x,t) - p_o = 4Eh(1 - \sqrt{A_o/A})/(3r_o) \tag{9}$$

where p_o is the zero transmural pressure or the diastolic pressure. For further convenience, these equations are nondimensionalized using the characteristic parameters $r_c = 1$ cm (characteristic radius of the vessels), $q_c = 10\ \mathrm{cm}^3.\mathrm{s}^{-1}$ (characteristic flow through the aorta) and $\rho = 1.06\ \mathrm{g.cm}^{-3}$ (density of blood). Thus, the following nondimensional quantities are defined. $\tilde{x} = x/r_c$, $\tilde{t} = tq_c/r_c^3$, $\tilde{r_o} = r_o/r_c$, $\tilde{A} = A/r_c^2$, $\tilde{q} = Q/q_c$, $\tilde{p} = pr_c^4/(\rho q_c^2)$, $\tilde{\nu} = \nu r_c/q_c$, $k_1 = k_1 r_c^4/(\rho q_c^2)$, $k_2 = k_2 r_c$ and $\tilde{k_3} = k_3 r_c^4/(\rho q_c^2)$. Using these quantities and by dropping tildes, the nondimensional continuity and momentum equations can be written as

$$\frac{\partial}{\partial t}\begin{pmatrix} A \\ q \end{pmatrix} + \frac{\partial}{\partial x}\begin{pmatrix} q \\ \frac{q^2}{A} + \frac{f}{\rho}\sqrt{A_o A} \end{pmatrix} = \begin{pmatrix} 0 \\ -\frac{2\pi r q}{\delta \Re A} + \left(2\sqrt{A}\left(\sqrt{\pi} f + \sqrt{A_o}\frac{df}{dr_o}\right) - A\frac{df}{dr_o}\right)\frac{dr_o}{dx} \end{pmatrix}. \tag{10}$$

C. Numerical Method

In this section a Richtmyer's two-step version of the Lax-Wendroff explicit scheme is described [2], [8]. The continuity and momentum equations should be in conservative form to numerically solve this second-order method. Let the dependent variables be represented by the vector

$$\mathbf{U} = (A, q) \tag{11}$$

the system flux by

$$\mathbf{F} = (F_1, F_2) = (q, q^2/A + f\sqrt{A_o A}/\rho) \tag{12}$$

and the right-hand side of (10) by

$$\mathbf{S} = (S_1, S_2) = \left(0, -\frac{2\pi r q}{\delta \Re A} + \left(2\sqrt{A}\left(\sqrt{\pi} f + \sqrt{A_o}\frac{df}{dr_o}\right) - A\frac{df}{dr_o}\right)\frac{dr_o}{dx}\right). \tag{13}$$

Thus, (10) becomes

$$\frac{\partial \mathbf{U}}{\partial t} + \frac{\partial \mathbf{F}}{\partial x} = \mathbf{S}. \tag{14}$$

By using an uniform grid, the flow at time-level $(n+1)$ and grid location m can be written as

$$\mathbf{U}_m^{n+1} = \mathbf{U}_m^n - \frac{\Delta t}{\Delta x}\left(\mathbf{F}_{m+\frac{1}{2}}^{n+\frac{1}{2}} - \mathbf{F}_{m-\frac{1}{2}}^{n+\frac{1}{2}}\right) + \frac{\Delta t}{2}\left(\mathbf{S}_{m+\frac{1}{2}}^{n+\frac{1}{2}} + \mathbf{S}_{m-\frac{1}{2}}^{n+\frac{1}{2}}\right) \tag{15}$$

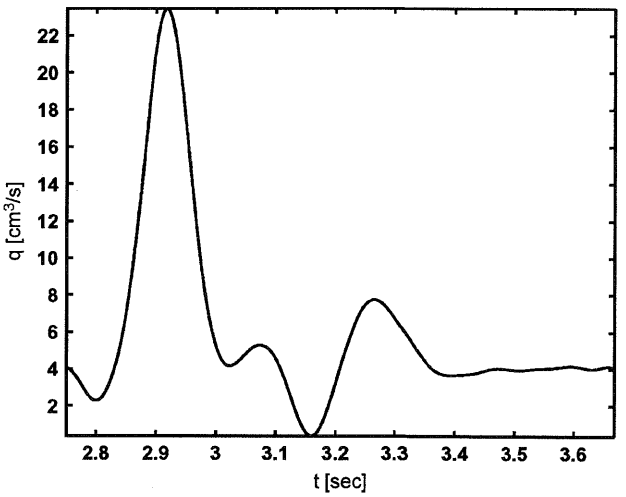

Fig. 2. Inflow as a function of time (Time period = 0.917 s). Obtained from the authors of [9].

where $\mathbf{U}_m^n = \mathbf{U}(m\Delta x, n\Delta t)$ and similarly for $\mathbf{F}$ and $\mathbf{S}$. The unknowns in the above equation $\mathbf{F}_{m+(1/2)}^{n+(1/2)}$, $\mathbf{F}_{m-(1/2)}^{n+(1/2)}$, $\mathbf{S}_{m+(1/2)}^{n+(1/2)}$ and $\mathbf{S}_{m-(1/2)}^{n+(1/2)}$ at time-level $(n + (1/2))$ can be determined using

$$\mathbf{U}_j^{n+\frac{1}{2}} = \frac{\mathbf{U}_{j+\frac{1}{2}}^n + \mathbf{U}_{j-\frac{1}{2}}^n}{2} + \frac{\Delta t}{2}\left(-\frac{\mathbf{F}_{j+\frac{1}{2}}^n - \mathbf{F}_{j-\frac{1}{2}}^n}{\Delta x} + \frac{\mathbf{S}_{j+\frac{1}{2}}^n + \mathbf{S}_{j-\frac{1}{2}}^n}{2}\right) \tag{16}$$

for $j = m + (1/2)$ and $j = m - (1/2)$. For an uniform grid, this method is stable if the CFL condition is fulfilled for both choices of sign, such that

$$\frac{\Delta t}{\Delta x} \leqslant \left|\frac{q}{A} \pm \sqrt{\frac{A}{\rho}\frac{\partial p}{\partial A}}\right|^{-1} \tag{17}$$

where q/A (Units - $\mathrm{cm.s}^{-1}$) is the mean velocity.

D. Boundary Conditions

The governing equations in (10) are quasilinear and hyperbolic in nature. One boundary condition is required at the end of any vessel since the characteristics point in opposite directions. The inflow boundary condition at the inlet of the common carotid artery (CCA) is determined using the periodic pulse function developed in [9] and shown in Fig. 2 as a function of time. At the inlet [e.g., Fig. 3(i)], (15) requires the evaluation of the term $q_{-(1/2)}^{n+(1/2)}$ using

$$q_0^{n+\frac{1}{2}} = \left(q_{-\frac{1}{2}}^{n+\frac{1}{2}} + q_{\frac{1}{2}}^{n+\frac{1}{2}}\right)/2 \tag{18}$$

where subscripts still signify the value of the spatial location. Also, from (15)

$$A_0^{n+1} = A_0^n - \Delta t\left((F_1)_{\frac{1}{2}}^{n+\frac{1}{2}} - (F_1)_{-\frac{1}{2}}^{n+\frac{1}{2}}\right)/\Delta x + \Delta t\left((S_1)_{\frac{1}{2}}^{n+\frac{1}{2}} - (S_1)_{-\frac{1}{2}}^{n+\frac{1}{2}}\right)/2 \tag{19}$$

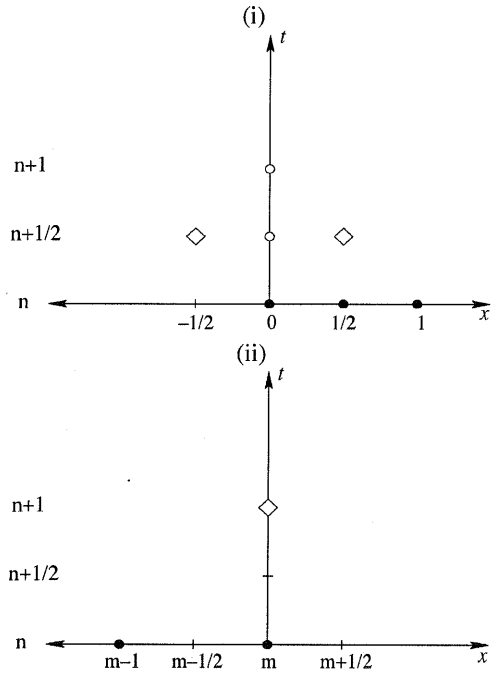

Fig. 3. Computational molecules (i) Left boundary: At points marked with '•', all variables are known, at points marked with 'o', the flow is known and at points marked with '◇', the variables are unknown. At time $n + (1/2)$, we determine the values of $q_{1/2}^{n+(1/2)}$ and A_0^{n+1} using (18) and (19), respectively. (ii) Right boundary: At points marked with '•', all variables are known and at point marked with '◇', the variables are unknown. Using fixed point iteration, with an initial guess on p_m^{n+1}, firstly, outlet flow at time $n+1$ is evaluated from Eqn. (30). Then the outlet area at time $n+1$ is evaluated using (31) and finally, outlet pressure at time $n+1$ is evaluated using (32).

where the inner subscripts on F and S denote the first row in (14) and $(S_1)_{1/2}^{n+(1/2)} = (S_1)_{-(1/2)}^{n+(1/2)} = 0$, $(F_1)_{1/2}^{n+(1/2)} = q_{1/2}^{n+(1/2)}$ and $(F_1)_{-(1/2)}^{n+(1/2)} = q_{-(1/2)}^{n+(1/2)}$. Fig. 3(i) shows the left boundary where the unknown variables at time step $(n+1)$ are evaluated from the known values at time steps n and $(n+(1/2))$. The unknown variables A_0^{n+1} and p_0^{n+1} are evaluated at the inlet as shown in Algorithm 1.

Algorithm 1. Steps for evaluating the variables at the inlet

Evaluate $q_0^{n+(1/2)}$ and q_0^{n+1} from the input pulse

Evaluate $q_{1/2}^{n+(1/2)}$ from (16)

Eliminate $q_{-(1/2)}^{n+(1/2)}$ in (19) from (18)

Evaluate A_0^{n+1} from (19)

Evaluate p_0^{n+1} from (9) where $m = 0$

The bifurcation occurs at a point where the outflow from the CCA is balanced with the inflow from the ICA and the external carotid artery (ECA). For simplicity, we use subscript p for the CCA, d_1 for the ICA and d_2 for the ECA for describing the bifurcation conditions. The evaluation of $\mathbf{F}_{\mathcal{M}+(1/2)}^{n-(1/2)}$, $\mathbf{F}_{\mathcal{M}+(1/2)}^{n+(1/2)}$, $\mathbf{S}_{\mathcal{M}+(1/2)}^{n-(1/2)}$ and $\mathbf{S}_{\mathcal{M}+(1/2)}^{n+(1/2)}$ requires introduction of ghost points at the outlet of the CCA and at the inlets of the ICA and ECA.

Note that $\mathcal{M} = M$ is the outlet grid point for the CCA and $\mathcal{M} = 0$ for the inlet grid points for the ICA and ECA. Using these ghost points, $(q^{(i)})_{\mathcal{M}}^{n+(1/2)}$ and $(A^{(i)})_{\mathcal{M}}^{n+(1/2)}$, where $i = p, d_1, d_2$, can be found as

$$\left(q^{(i)}\right)_{\mathcal{M}}^{n+\frac{1}{2}} = \left(\left(q^{(i)}\right)_{\mathcal{M}-\frac{1}{2}}^{n+\frac{1}{2}} + \left(q^{(i)}\right)_{\mathcal{M}+\frac{1}{2}}^{n+\frac{1}{2}}\right)/2 \tag{20}$$

and

$$\left(A^{(i)}\right)_{\mathcal{M}}^{n+\frac{1}{2}} = \left(\left(A^{(i)}\right)_{\mathcal{M}-\frac{1}{2}}^{n+\frac{1}{2}} + \left(A^{(i)}\right)_{\mathcal{M}+\frac{1}{2}}^{n+\frac{1}{2}}\right)/2 \tag{21}$$

respectively.

The bifurcation conditions, at time levels $(n + (1/2))$ and $(n + 1)$ lead to the following equations. Conservation of flow gives

$$\left(q^{(p)}\right)_M^j = \left(q^{(d_1)}\right)_0^j + \left(q^{(d_2)}\right)_0^j \tag{22}$$

and assumption of continuous pressure across the bifurcation gives

$$\left(p^{(p)}\right)_M^j = \left(p^{(d_1)}\right)_0^j = \left(p^{(d_2)}\right)_M^j \tag{23}$$

where $j = (n + (1/2)), (n + 1)$. Using (9), (23) can be written as

$$\left(f^{(p)}\right)_M \left(1 - \sqrt{\frac{\left(A_0^{(p)}\right)_M}{\left(A^{(p)}\right)_M^{n+\frac{1}{2}}}}\right) = \left(f^{(d_i)}\right)_0 \left(1 - \sqrt{\frac{\left(A_0^{(d_i)}\right)_0}{\left(A^{(d_i)}\right)_0^{n+\frac{1}{2}}}}\right) \tag{24}$$

and

$$\left(f^{(p)}\right)_M \left(1 - \sqrt{\frac{\left(A_0^{(p)}\right)_M}{\left(A^{(p)}\right)_M^{n+1}}}\right) = \left(f^{(d_i)}\right)_0 \left(1 - \sqrt{\frac{\left(A_0^{(d_i)}\right)_0}{\left(A^{(d_i)}\right)_0^{n+1}}}\right) \tag{25}$$

where $i = d_1, d_2$ and $f(r_o) = 4Eh/(3r_o)$. For $i = d_1, d_2$, (15) can be written for q and A as

$$\left(q^{(i)}\right)_{\mathcal{M}}^{n+1} = \left(q^{(i)}\right)_{\mathcal{M}}^{n} - \frac{\Delta t}{\Delta x}\left(\left(F_2^{(i)}\right)_{\mathcal{M}+\frac{1}{2}}^{n+\frac{1}{2}} - \left(F_2^{(i)}\right)_{\mathcal{M}-\frac{1}{2}}^{n+\frac{1}{2}}\right) + \frac{\Delta t}{2}\left(\left(S_2^{(i)}\right)_{\mathcal{M}+\frac{1}{2}}^{n+\frac{1}{2}} + \left(S_2^{(i)}\right)_{\mathcal{M}-\frac{1}{2}}^{n+\frac{1}{2}}\right) \tag{26}$$

TABLE I
GEOMETRY OF THE CCA, ICA AND ECA (UNITS: cm)

	r_u	r_d	L
CCA	0.370	0.370	20.8
ICA	0.177	0.083	17.6
ECA	0.177	0.083	17.7

and

$$\left(A^{(i)}\right)_{\mathcal{M}}^{n+1} = \left(A^{(i)}\right)_{\mathcal{M}}^{n} - \frac{\Delta t}{\Delta x}\left(\left(F_1^{(i)}\right)_{\mathcal{M}+\frac{1}{2}}^{n+\frac{1}{2}} - \left(F_1^{(i)}\right)_{\mathcal{M}-\frac{1}{2}}^{n+\frac{1}{2}}\right) \tag{27}$$

as $S_1 = 0$. Eqns. (20) to (27) comprising the unknowns $(q^{(p)})_M^{n+1}$, $(q^{(p)})_M^{n+(1/2)}$, $(q^{(p)})_{M+(1/2)}^{n+(1/2)}$, $(q^{(d_1)})_0^{n+1}$, $(q^{(d_1)})_0^{n+(1/2)}$, $(q^{(d_1)})_{-(1/2)}^{n+(1/2)}$, $(q^{(d_2)})_0^{n+1}$, $(q^{(d_2)})_0^{n+(1/2)}$, $(q^{(d_2)})_{-(1/2)}^{n+(1/2)}$, $(A^{(p)})_M^{n+1}$, $(A^{(p)})_M^{n+(1/2)}$, $(A^{(p)})_{M+(1/2)}^{n+(1/2)}$, $(A^{(d_1)})_0^{n+1}$, $(A^{(d_1)})_0^{n+(1/2)}$, $(A^{(d_1)})_{-(1/2)}^{n+(1/2)}$, $(A^{(d_2)})_0^{n+1}$, $(A^{(d_2)})_0^{n+(1/2)}$, and $(A^{(d_2)})_{-(1/2)}^{n+(1/2)}$ give rise to a system of 18 nonlinear equations which can be solved using Newton's method only if the Jacobian is nonsingular [2], [8].

For the outflow boundary condition at the outlets of the ICA and ECA, a three-element Windkessel model [1] based on wave transmission theory is used which represents the resistance of the vessel by two resistances R_1, R_2 and the compliance of the vessel by a capacitor C_T. At a frequency ω, the impedance of this model is given by

$$Z(0,\omega) = \frac{R_1 + R_2 + i\omega C_T R_1 R_2}{1 + i\omega C_T R_2}. \tag{28}$$

Transforming (28) into the time domain gives the following partial differential equation

$$\frac{\partial p}{\partial t} = R_1 \frac{\partial q}{\partial t} - \frac{p}{R_2 C_T} + \frac{q(R_1 + R_2)}{R_2 C_T}. \tag{29}$$

The above equation can be written in discretized form as

$$\frac{p_m^{n+1} - p_m^n}{\Delta t} = R_1 \frac{\left(q_m^{n+1} - q_m^n\right)}{\Delta t} - \frac{p_m^n}{R_2 C_T} + \frac{q_m^n (R_1 + R_2)}{R_2 C_T}. \tag{30}$$

Note that the treatment here of the outflow boundary condition is different when compared to the one used in [8]. Also, by discretising the mass conservation equation, we get

$$A_m^{n+1} = A_m^n - \Delta t \left(q_m^{n+1} - q_{m-1}^{n+1}\right)/\Delta x. \tag{31}$$

In order to determine the unknowns at the outlet [e.g., Fig. 3(ii)], (30), (31) and the discretized state equation

$$p_m^{n+1} = \frac{4}{3}\frac{Eh}{r_o}\left(1 - \sqrt{\frac{A_o}{A_m^{n+1}}}\right) \tag{32}$$

are solved using a fixed-point iterative scheme by starting with an initial guess for p_m^{n+1} on each vessel. Fig. 3(ii) shows the right boundary where the unknown variables at the time step $(n+1)$ are evaluated as shown in Algorithm 2 using the known values at the time step n.

Algorithm 2. Steps for evaluating the variables at the outlet using fixed point iteration

$p_m^{n+1} = p_m^n$.
$k = 0$.
while $k \leqslant k_{max}$ **do**
  $p_{old} = p_m^n$
  Evaluate q_m^{n+1} from (30)
  Evaluate A_m^{n+1} from (31)
  Evaluate p_m^{n+1} from (32)
  if $|p_{old} - p_m^{n+1}| < 10^{-7}$ **then**
    break
  end if
  $k = k + 1$.
end while

III. RESULTS AND DISCUSSION

A. Preliminary Simulations

At the outset, mesh and time dependence studies are performed for flow in the 1-D human carotid artery bifurcation. The physiological data taken for this study is based upon the data described in [1], [8] and [10]. The geometry of the CCA, ICA and ECA branches is summarized in Table I. Note that L refers to the length of a vessel, r_u and r_d signify the upstream and downstream cross-sections of a vessel, respectively. It is worth noting here that in order to avoid simultaneous interactions between the reflected waves, the difference in the lengths of the ECA and ICA is taken as 0.1 cm [10]. Time period $T = 0.917$ s is the period of one cycle and the kinematic viscosity $\nu = 0.046\ \text{cm}^2.\text{s}^{-1}$. The values R_1, R_2 and C_T for the outflow boundary condition are empirically estimated (so that there is no pressure buildup after each cycle) and tabulated in Table II. Furthermore, the wall thickness (h) and the Young's modulus (E) are calculated from the empirically estimated (4). Also, the numerical method discussed in the previous sections has been validated for a single vessel in [11]. We start the computations by initialising values for all the variables in the first cycle. Hence, the pressure and flow profiles obtained at the end of the first cycle are not immediately reliable. Therefore, the model needs a few periods to stabilise itself [8]. Henceforth, all the numerical computations in this study are performed for four cycles and the data was extracted for the fourth cycle.

Fig. 4 shows plots for three cases obtained by successively doubling the grid points and the number of time steps starting from an initial configuration having the space step $\Delta x = 0.2$ cm and time step $\Delta t = 0.00002$ s. Although the plots for all the three cases overlap each other for the ICA and the ECA, by

TABLE II
OUTFLOW CONSTANTS

R_1	R_2	C_T
13900 $g.s^{-1}.cm^{-4}$	25300 $g.s^{-1}.cm^{-4}$	1.3384×10^{-6} $cm^4.s^2.g^{-1}$

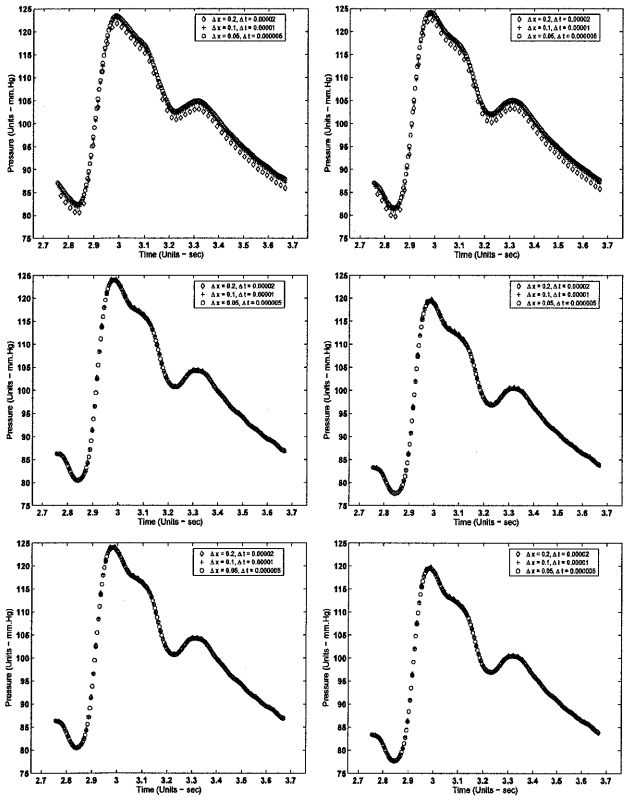

Fig. 4. Mesh and time dependence results for the carotid bifurcation. The first row are the plots for the CCA at locations 6.0 cm and 12.0 cm respectively. Similarly, in the second row, plots for the ICA are shown at locations 6.0 cm and 12.0 cm respectively. Finally, in the third row, plots for the ECA are shown at the same locations. Units for Δx - cm and for Δt - sec.

closer inspection, it can be seen that only the plots for the last two cases overlap each other for the CCA. Hence, we decided to choose the configuration with $\Delta x = 0.1$ cm and $\Delta t = 0.00001$ s for all the subsequent simulations on the bifurcation. Fig. 5 shows the variation of pressure in the CCA, ICA and ECA, respectively, as a function of space and time. The pressure profiles of the CCA have all the characteristics as depicted in [2]. Additionally, we show the pressure profiles of the ICA and the ECA by extending the numerical analysis to the bifurcation.

B. Stenosis Model

Surgical decisions are often made with regard to when and how to treat a particular patient depending upon the degree of stenosis. This is observed on crude observational data of the correlation of angiographically or ultrasound derived assessment of stenosis. Provision of better understanding of haemodynamics of a stenotic vessel will enhance the conventional wisdom regarding these decisions. Therefore, we introduce a metric, PVF

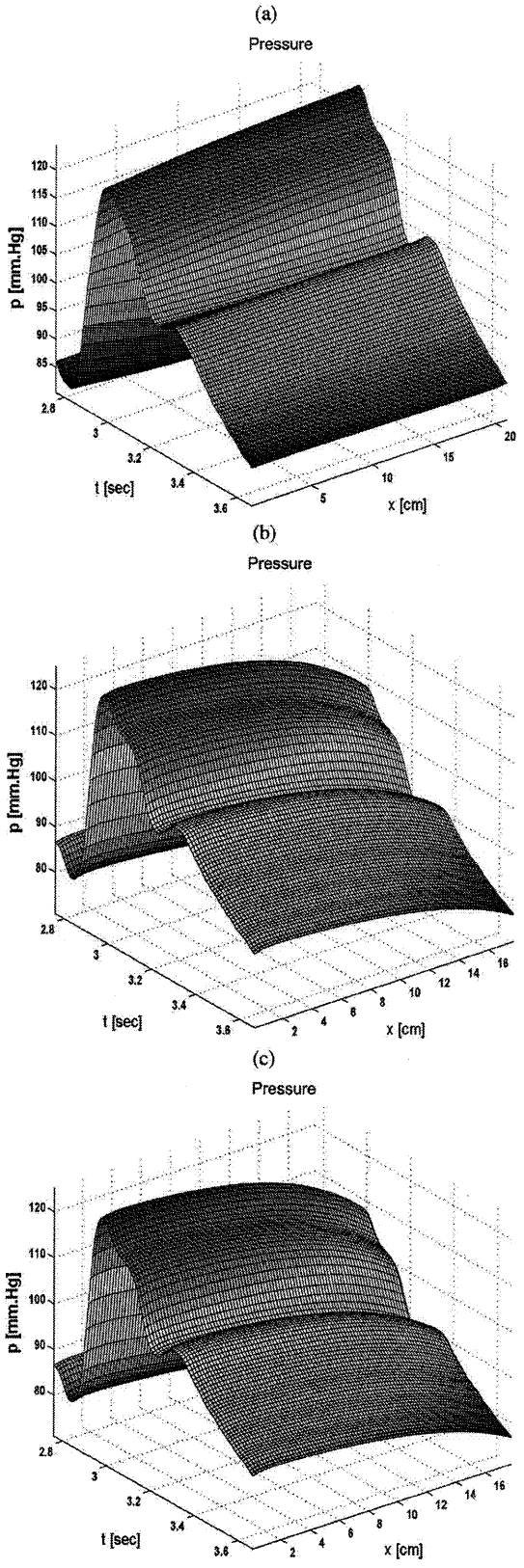

Fig. 5. Variation of pressure along the (a) common carotid, (b) internal carotid and the (c) external carotid arteries, respectively, as a function of the length of the corresponding vessel (x [cm]) and time (t [sec]) in the fourth cycle. Each of the contour plots are shown from the inlet to the outlet of each vessels, respectively.

and thereby provide a new indicator for analysing the flow behavior. It is defined as

$$\text{PVF} = \left(\int_{t}^{t+jT} \int_{0}^{L} (p_s - p)^2 dx dt \right) / \left(\int_{t}^{t+jT} \int_{0}^{L} p^2 dx dt \right) \tag{33}$$

where $p_s(x, t + jT) = p_s(x, t)$ and $p(x, t + jT) = p(x, t)$ (for $j = 1, 2, 3, \ldots$) are respectively, the instantaneous pressure in the presence of a stenosis and the instantaneous pressure when there is no stenosis. This nondimensional metric quantifies the extent of deviation of pressure from ideal behavior in the entire cross-section of the vessel. Clearly, positive and negative changes in local pressure will affect PVF equally but we are concerned with a measure of global variations.

Additionally, the nondimensional value of maximum pressure

$$p_m^* = (\text{Max}\,[p_s(x,t)])\,/\,(\text{Max}\,[p(x,t)]) \tag{34}$$

was extracted for each case to gain a better insight into the problem. The underlying assumption is that the metric PVF will account for the global changes in the pressure whereas p_m^* is more local and hence provides an estimate of the peak pressure increment. Empirical stenosis models in previous studies [1], [3] were used to incorporate the flow behavior through the stenosis. However, in the present study, the governing equations described in the previous section are numerically solved to study the flow for all degrees of stenoses. It is believed that the gross effects of the disease can be correctly captured through these metrics. The area stenosis is modelled using a Hicks-Henne bump function [12] which is defined as

$$r'(x) = a sin\left(\pi x^{\frac{log 0.5}{log t_1}}\right)^{t_2};\ \text{for}\ 0 \leqslant x \leqslant 1 \tag{35}$$

where $r'(x)$ controls the radius of the vessel, a is the maximum bump magnitude, t_1 controls the location of the maximum point of the bump and t_2 controls the width of the bump. Fig. 6 shows different shapes of stenoses obtained by varying the parameters in (35) and for different tapering factors [e.g., (2)]. With reference to the radius of the arterial vessel $(r(x))$ defined in (1), the effective radius of the vessel becomes

$$r_e(x) = r(x) - r'(x). \tag{36}$$

In accordance with this definition, the percentage of area stenosis (as used in [1]) can be evaluated as

$$P_{as} = \left(1 - r_e^2(x)/r^2(x)\right) \times 100. \tag{37}$$

It should be noted that the parameter a directly controls the percentage of area reduction of the vessel and hence for obtaining physiologically realistic geometries, it should vary within $[0, r(x)]$ cm. t_1 is however a nondimensionalized parameter with respect to the length of the vessel and hence it varies within [0,1]. Furthermore, since t_2 appears as an exponent, it takes any value ≥ 0. Note that as t_2 increases, the extent of stenosis decreases.

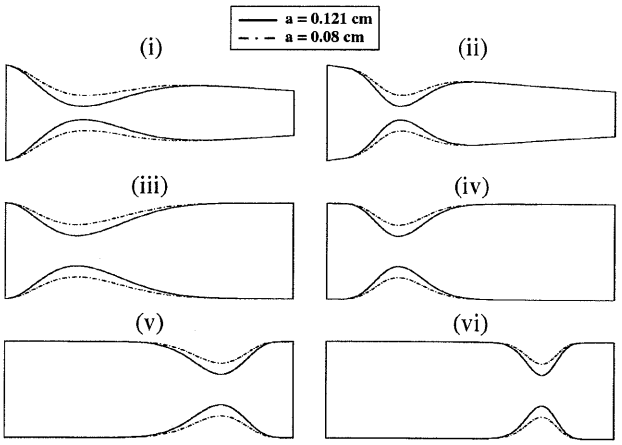

Fig. 6. Two dimensional illustrations of the shapes of stenosis in the ICA for different values of a, t_1 and t_2 in the Hicks-Henne bump function defined in (35). (i) $k = -0.043\ \text{cm}^{-1}$, $t_1 = 0.25$, $t_2 = 5.0$, (ii) $k = -0.043\ \text{cm}^{-1}$, $t_1 = 0.25$, $t_2 = 15.0$, (iii) $k = 0\ \text{cm}^{-1}$, $t_1 = 0.25$, $t_2 = 5.0$, (iv) $k = 0\ \text{cm}^{-1}$, $t_1 = 0.25$, $t_2 = 15.0$, (v) $k = 0\ \text{cm}^{-1}$, $t_1 = 0.75$, $t_2 = 5.0$ and (vi) $k = 0\ \text{cm}^{-1}$, $t_1 = 0.75$, $t_2 = 15.0$. In all the subplots, the dotted line denotes the shape for 70% area stenosis and the solid line denotes the shape for 90% area stenosis. k denotes the tapering factor defined in (2). The length of the vessel $L = 17.6$ cm and the inlet radius $r_u = 0.177$ cm.

First, we computed pressure and flow in the ICA by assuming the tapering factor $k = 0$ for all the vessels and without any stenosis. We keep these values of pressure and flow as the reference values (with no stenosis) for computing PVF and p_m^* in the subsequent studies. Later, for exploring the effect of changes in a, t_1 and t_2 on PVF and p_m^*, the Hicks-Henne function's parameters are varied as $a \in [0, 0.177]$ cm (so that the maximum bump magnitude is not greater than the cross-section of the ICA), $t_1 \in [0, 1]$ (so that the peak of the stenosis occurs within the upstream and downstream ends of the ICA) and $t_2 \in [0, 17.6]$ (so that spiky stenosis shapes are avoided) only for the ICA keeping the geometry of the CCA as $r_u = 0.37$ cm, $r_d = 0.37$ cm and $L = 20.8$ cm and the ECA as $r_u = 0.177$ cm, $r_d = 0.177$ cm and $L = 17.7$ cm. Note that the stenosis is imposed on the ICA geometry which has $r_u = 0.177$ cm, $r_d = 0.177$ cm and $L = 17.6$ cm. In so doing, several geometries with varying degrees and shapes of stenoses in the ICA (or design points) are created and a parametric analysis is conducted to understand the behavior of PVF. For systematic exploration of the influence of the shape of stenosis on PVF, a design of experiments (DoE) technique was employed to generate 100 geometries [13], [14]. The DoE technique used in this paper is a well known method in the field of aerospace design and is used to populate an n-dimensional space by maximising the minimum distance between two design points. Due to the high perturbations assumed for the parameters, numerical simulations were feasible on only 84 geometries.

By observing the plots of the first row in Fig. 7, we see that PVF reaches its maximum value when the location of the peak of stenosis is in the upstream segment of the ICA ($t_1 < 0.5$). This

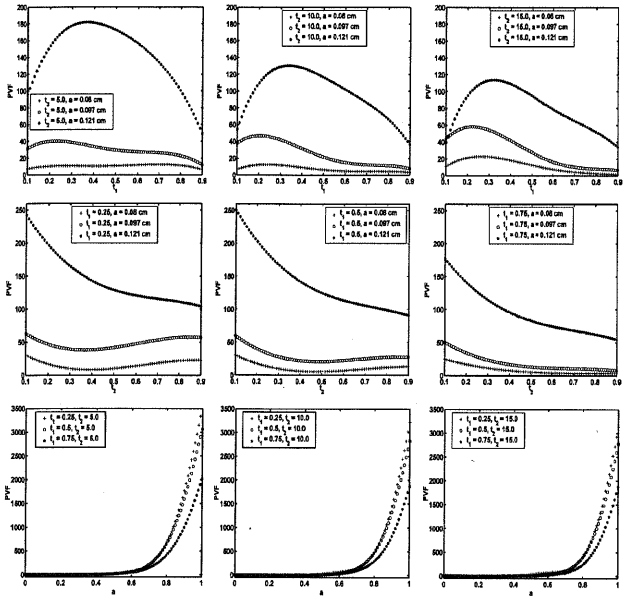

Fig. 7. Variation of PVF for different values of the Hicks-Henne bump function parameters. In all the subplots PVF is shown along the y-axis. In the first row, t_1 is plotted along the x-axis for different values of a and t_2. In the second row, t_2 is plotted along the x-axis for different values of a and t_1. In the third row, a is plotted along the x-axis for different values of t_1 and t_2. All the parameters are appropriately normalized using their lower and upper bounds. Note that value of $a = 0.08$ cm corresponds to 70% area stenosis in the ICA, $a = 0.097$ cm corresponds to 80% area stenosis and $a = 0.121$ cm corresponds to 90% area stenosis.

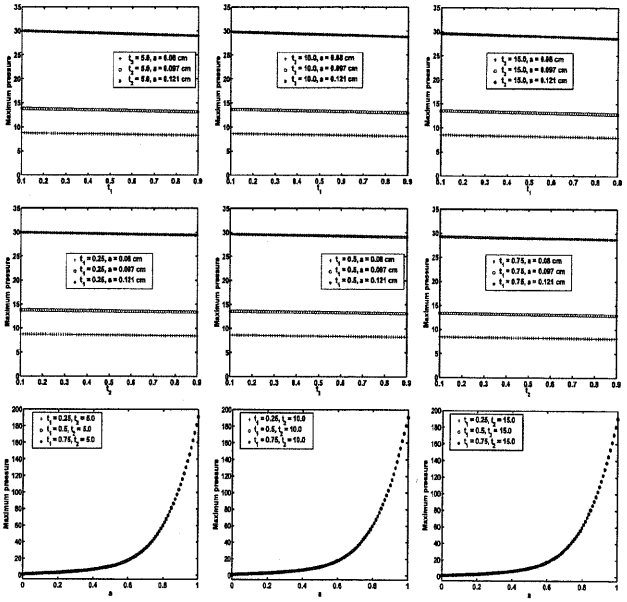

Fig. 8. Variation of p_m^* for different values of the Hicks-Henne bump function parameters. In all the subplots p_m^* is shown along the y-axis. In the first row, t_1 is plotted along the x-axis for different values of a and t_2. In the second row, t_2 is plotted along the x-axis for different values of a and t_1. In the third row, a is plotted along the x-axis for different values of t_1 and t_2. All the parameters are appropriately normalized using their lower and upper bounds. Note that value of $a = 0.08$ cm corresponds to 70% area stenosis in the ICA, $a = 0.097$ cm corresponds to 80% area stenosis and $a = 0.121$ cm corresponds to 90% area stenosis.

may also imply that the probability of an overall catastrophic effect such as plaque rupture is greater when the peak of stenosis is further upstream in the ICA. Furthermore, from the second row in Fig. 7, it can be clearly seen that PVF reaches its peak value when the extent of stenosis is maximum. From the third rows in Figs. 7 and 8, we see that PVF and p_m^* increase with the parameter a which directly suggests that they are directly proportional to the percentage of stenosis. It can be seen that from the first and second rows of Fig. 8 that p_m^* is almost insensitive to changes in t_1 and t_2. A possible inference from this observation is that local catastrophic effects do not depend on the extent of stenosis and the location of the peak of stenosis.

C. Stent Implanted Model

Now we consider a case where a stent is inserted in the region of a stenosis to recover the shape of the original vessel and reduce the stenosis imposed by arterial disease. The geometry for this case is shown in Fig. 9. As before, for both ICA and ECA $r_u = r_d = 0.177$ cm and for the CCA $r_u = r_d = 0.37$ cm. Also, the radius of the stent is taken as $r_s = 0.177$ cm. In this study, we determine the elasticity of the vessel from estimates of Young's modulus (E), the radius (r_o) and the wall thickness (h) from (4). We assume that a stent of length l_s is placed in the region $x \in [\Delta, l_s + \Delta]$. For the region of increased stiffness, the effective Young's modulus (E_s) is 5×10^8 g.cm^{-1}.s^{-2} and the stent strut thickness is 0.01 cm [11]. The elasticity along the length of the vessel is defined in (38), at the bottom of the next page, where L_{ICA} is the length of the ICA, and the cubic polynomial coefficients are employed

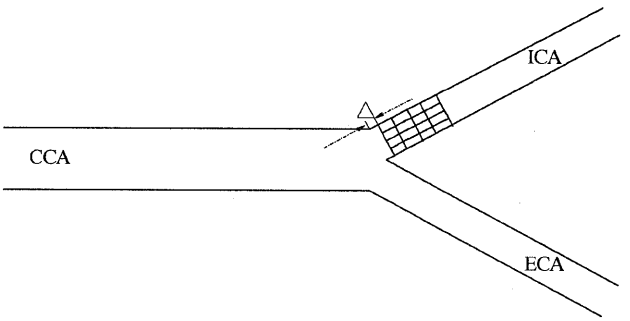

Fig. 9. Schematic of the 1-D human carotid artery bifurcation with a stent of length l_s placed in the ICA. Dimensions of the CCA are $r_u = 0.37$ cm, $r_d = 0.37$ cm and $L = 20.8$ cm; for the ICA $r_u = 0.177$ cm, $r_d = 0.177$ cm and $L = 17.6$ cm and for the ECA $r_u = 0.177$ cm, $r_d = 0.177$ cm, and $L = 17.7$ cm.

to represent the elasticity along the length of the vessel based on the work by Sherwin *et al.* (2003) [4]. Also, the value of Δ for this case is taken as $l_s/10$. For exploring the impact of variations in l_s and E_s on PVF and p_m^* respectively, 100 geometries are created using a DoE technique [13], [14] to explore the effect of varying $l_s \in [0, 17.6]$ cm and $E_s \in [2.5 \times 10^8, 7.5 \times 10^8]$ g.cm^{-1}.s^{-2}. For this problem, the variables with a subscript s in (33) and (34) signify cases where there is a stent placed inside the vessel and the variables without any subscript denote cases where there is no stent or stenosis inside the vessel. Fig. 10(A) depicts the complex behavior of PVF in which the metric is found to be more sensitive to variations in E_s than l_s for $l_s \gtrapprox 0.8$. In contrast, for $l_s \lessapprox 0.5$ and $E_s \gtrapprox 0.5$, it can be seen that variations in E_s influence the metric more

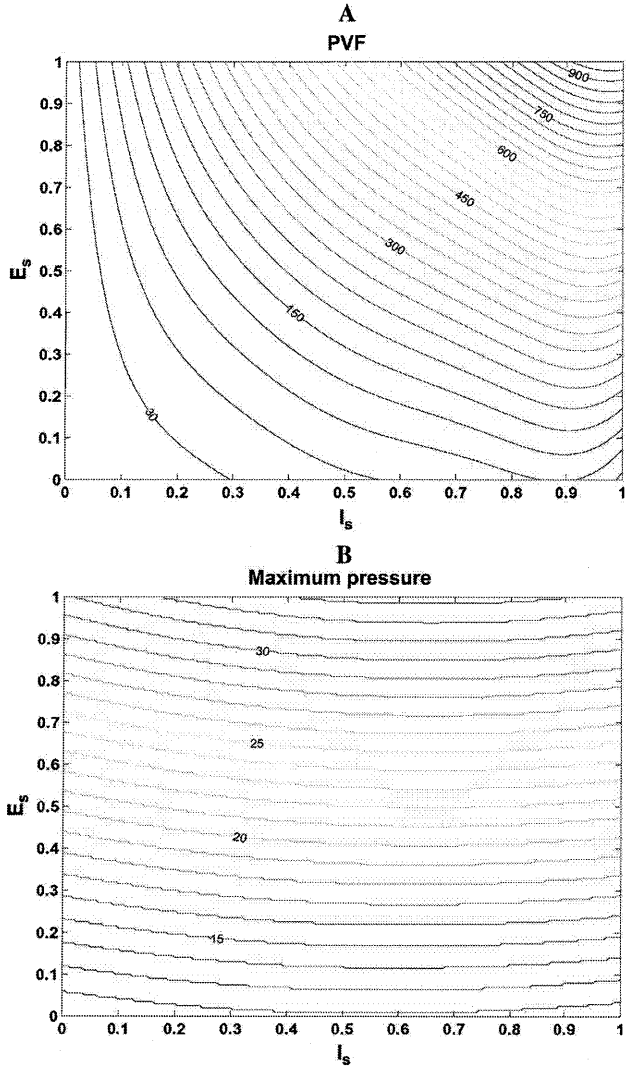

Fig. 10. (A) Variation of PVF with respect to l_s and E_s and (B) Variation of p_m^* with respect to l_s and E_s. Note that l_s and E_s are appropriately normalized using their lower and upper bounds respectively. PVF and p_m^* are calculated as the increment in global and local pressures with respect to the healthy carotid bifurcation and by choosing a tapering factor $k = 0\ \mathrm{cm}^{-1}$.

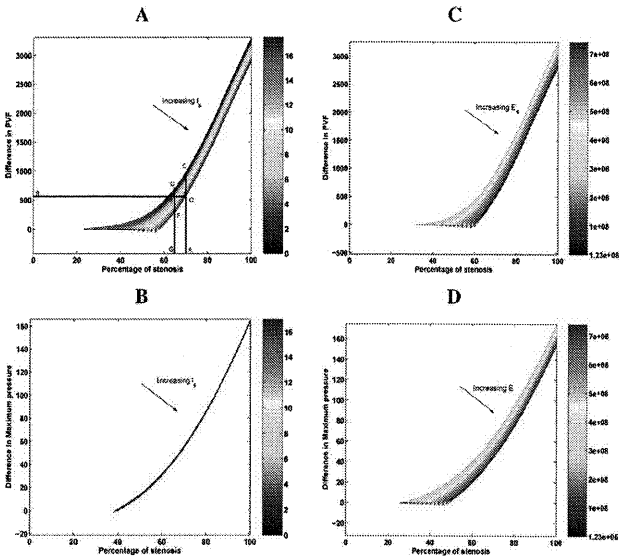

Fig. 11. Case 1: $t_1 = 0.25$ and $t_2 = 5.0$. (A) and (B) Predictions on the length (Units - cm) of the stent for varying degrees of stenosis. (C) and (D) Predictions on the Young's modulus of the stent (Units - $\mathrm{g.cm^{-1}.s^{-2}}$) for varying degrees of stenosis. On the y-axis of (A) and (C), $\Delta\mathrm{PVF} = \mathrm{PVF}_{\mathrm{stenosis}} - \mathrm{PVF}_{\mathrm{stent}}$ and on the y-axis of (B) and (D), $\Delta p_m^* = p_{m_{\mathrm{stenosis}}}^* - p_{m_{\mathrm{stent}}}^*$.

than the changes in l_s. Much simpler behavior is manifested by p_m^* as shown in Fig. 10(B) in which the metric is less sensitive to variations in l_s than E_s. This observation directly suggests that localized pressure peaks can be generated due to the presence of even an infinitesimally short length of a body which has low compliance relative to the arterial wall.

D. Test Problems

So far, this work has investigated the variation of pressure-based metrics through stenosed and stent-implanted arterial bifurcations. We now hypothesize that stent implantation may be beneficial if it reduced the magnitude of these metrics. In practice, diagnostic information could be provided for individual subjects with a certain degree of stenosis by first evaluating the values of PVF and p_m^* in a model of the stenosed geometry and then selecting a stent with suitable l_s and E_s, only if the corresponding metrics are reduced after the insertion. To make the model patient-specific, powerful tools such as magnetic resonance imaging (MRI) techniques can be used for extracting realistic geometries, inflow and outflow boundary conditions [15], [16]. To demonstrate the range of applicability of this approach, a test case is conducted using the Hicks-Henne function with the parameters t_1 and t_2 [e.g., (35)] fixed at 0.25 and 5.0, respectively, representing a stenosis closer to the entrance of the ICA [e.g., Fig. 6(iii)]. The values of PVF and p_m^* are extracted for varying degrees of area stenosis first for a fixed value of $E_s = 5 \times 10^8\ \mathrm{g.cm^{-1}.s^{-2}}$ and then for a fixed value of $l_s = 8.8\ \mathrm{cm}$. Fig. 11 shows the variation of l_s and E_s plotted for positive differences in PVF and p_m^* against percentage of area stenosis. Recall that the differences in the metrics indicate their changes after subsequent insertion of the stent. The evidence

$$\frac{Eh}{r_o} = \begin{cases} (-99.545x^3 + 119.45x^2 + 1.1658) \times 10^4 & \forall \quad x \in [0, 2\Delta] \\ 2.8249 \times 10^7 & \forall \quad x \in [2\Delta, l_s] \\ (9.9545x^3 - 131.4x^2 + 573.38x - 825.55) \times 10^5 & \forall \quad x \in [l_s, l_s + 2\Delta] \\ 1.2358 \times 10^6 & \forall \quad x \in [l_s + 2\Delta, \mathrm{L_{ICA}}] \end{cases} \mathrm{g.cm^{-1}.s^{-2}} \tag{38}$$

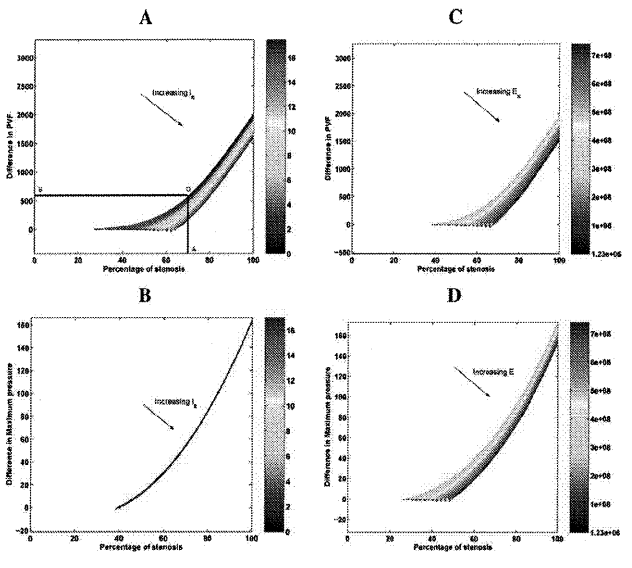

Fig. 12. Case 2: $t_1 = 0.75$ and $t_2 = 5.0$. (A) and (B) Predictions on the length (Units - cm) of the stent for varying degrees of stenosis. (C) and (D) Predictions on the Young's modulus of the stent (Units - $\mathrm{g.cm^{-1}.s^{-2}}$) for varying degrees of stenosis. On the y-axis of (A) and (C), $\Delta\mathrm{PVF} = \mathrm{PVF}_{\mathrm{stenosis}} - \mathrm{PVF}_{\mathrm{stent}}$ and on the y-axis of (B) and (D), $\Delta p^*_m = p^*_{m_{\mathrm{stenosis}}} - p^*_{m_{\mathrm{stent}}}$.

from clinical studies suggests that intervention (surgery or stent deployment) may be beneficial if the stenosis $\geq$70%. This principle may not be entirely general as it does not specifically account for the haemodynamic changes inside the arterial vessel. The computational study presented here offers guidelines which are physiologically reasonable and can be used in conjunction with the clinical indication to provide additional validation for a surgical decision. For example, it can be seen from Fig. 11(A) that intervention could be beneficial (as measured by a positive $\Delta\mathrm{PVF} = \mathrm{PVF}_{\mathrm{stenosis}} - \mathrm{PVF}_{\mathrm{stent}}$) for stenotic geometries whose percentage of area stenosis $\gtrapprox$23. Furthermore, if the percentage of area stenosis $\gtrapprox$60, then a stent which can cover the entire length of the vessel could also be chosen. However, clinical factors may demand a higher threshold for ΔPVF precluding stent implantation below this level. Consider the line OB [Fig. 11(A)] indicating the threshold value at percentage of area stenosis = 70. Hence, for all stenoses $\in [23, 70]$%, the range for the length of the stent is reduced. For example, the suitable range at 65% area stenosis is now DE as opposed to DF. The limited range for l_s [Fig. 11(B)] confirms the inference made from the second plot of Fig. 10 that p^*_m is less sensitive towards variations in the length of the stent. Fig. 11(C) and (D) shows a suitable range of Young's modulus for a fixed l_s of 8.8 cm. In this paper, it is assumed that the Young's modulus of any stent cannot be less than that of the arterial wall. Fig. 11(C) shows that any value of E_s within the bounds can be chosen for the stent if the percentage of area stenosis $\gtrapprox$60. Furthermore, from Fig. 11(D), we can infer that if percentage of area stenosis $\gtrapprox$50, then any value of E_s will give rise to positive differences in $\Delta p^*_m = p^*_{m_{\mathrm{stenosis}}} - p^*_{m_{\mathrm{stent}}}$. Another test case is considered with the parameters t_1 and t_2 fixed at 0.75 and 5.0, respectively, representing a stenosis closer to the downstream end of the ICA [e.g., Fig. 6(v)]. By considering the same threshold (indicated as OB in Fig. 12(A) as taken for the previous test case [e.g., Fig. 11(A)], we see that stent implantation may not be favorable even at 70% area stenosis. Fig. 12(B) also confirms that p^*_m is less sensitive towards variations in the length of the stent. Since the location of the peak of stenosis is closer to the downstream of the ICA for this case, the option of choosing any value of E_s within the bounds is now possible only if the percentage of area stenosis $\gtrapprox$70 and not 60 [e.g., Figs. 11(C) and 12(C)]. Contrastingly, Figs. 11(D) and 12(D) reveal the same observation regarding positive differences in Δp^*_m.

It can be clearly seen from Figs. 11 and 12 that ΔPVF and Δp^*_m increase with the percentage of stenosis. An interesting observation which can be derived from these figures is that for a given percentage of stenosis, ΔPVF and Δp^*_m need to be as high as possible which may allow the possibility of choosing a stent configuration that has minimum values for the length and Young's modulus. It should be noted that these ranges are predicted by only accounting for the pressure changes in the ICA. Additional information involving the pressure changes in the CCA and the ECA can be found in a similar fashion which gives rise to six exclusive indicators. For a given patient, we could propose a score based on whether there would be an increase or a decrease in each of these metrics after stent deployment, and suitable values of E_s and l_s could be extracted. Alternatively, stratification by these predictive scores can be helpful for determining the likely overall benefit from stenting and drawing conclusions on the efficacy of surgery [17].

IV. Conclusion

A 1-D time dependent Navier-Stokes solver incorporating fluid-wall interactions was implemented for studying blood flow in the human carotid artery bifurcation. A design of experiments technique was used to create geometries for a parametric study in order to investigate the alterations in pressure profiles due to the presence of a stenosis in the ICA. The stenotic geometry was parameterized using a Hicks-Henne bump function. We introduced a PVF as a metric for quantifying global alterations in haemodynamics due to changes in the stenotic geometry. It was shown that the probability of an overall catastrophic effect may be higher when the stenosis is located in the upstream segment of the internal carotid. For quantifying local changes in the haemodynamics, maximum pressure was used as the metric. This metric was found to be less sensitive towards variations in the location of the peak and extent of stenosis. Furthermore, we showed how these metrics respond after stent deployment into the stenosed part of the internal carotid. In particular, it was shown that localized pressure peaks may be generated even in the presence of an infinitesimally short length of a stent. Finally, we proposed and discussed potential diagnostic tools based on these parametric analyses and demonstrated how they could be used (once they have been shown to accurately predict arterial behavior through experimental validation) as cost effective methods to predict the effect of stenting for an individual patient rather than relying solely on the percentage of stenosis in a vessel. It is worth noting here that although PVF quantifies the global increment in pressure, both positive and negative changes in local pressure will affect PVF equally whereas it might be thought that positive and negative pressures will have different

effects on the physiology of the artery. We hope to look into these differences in our future work.

These studies can be further benefited by considering additional aspects of stent design methodology such as risk factor modelling, cost-effectiveness of this procedure and comparing the scope of stenting with other available interventional techniques [17], [18]. Most importantly, these simplified models can be used in a multi-scale approach to represent the global dynamics of the arterial system where detailed three dimensional simulations are used only in regions which are of particular interest [19]. However, in addition to the need for experimental validation, the 1-D model will require verification against 3-D simulations; a key weakness of the lower fidelity model used here concerns the inability to predict shear stress, separation, and energy loss due to vorticity. Nonetheless, the approach presented in this paper highlights the potential usefulness of a parametric study and its subsequent application to predict the benefit of stenting in a diseased patient. Alternatively, statistical techniques [14] which can reasonably quantify the uncertainty involved with inter/intra individual differences in the geometry and material properties could be used.

ACKNOWLEDGMENT

The authors would like to thank the reviewers for their comments and suggestions. This research was performed during V. B. Kolachalama's doctoral study and he would like to thank the School of Engineering Sciences at the University of Southampton for providing a studentship. V. B. Kolachalama would also like to thank Prof. M. S. Olufsen, NCSU, for useful discussions on the implementation of the scheme.

REFERENCES

[1] N. Stergiopulos, D. F. Young, and T. R. Rogge, "Computer simulation of arterial flow with applications to arterial and aortic stenoses," *J. Biomech.*, vol. 23, no. 1, pp. 1477–1488, 1992.

[2] M. S. Olufsen, C. S. Peskin, W. Y. Kim, E. M. Pederson, A. Nadim, and J. Larsen, "Numerical simulation and experimental validation of blood flow in arteries with structured tree outflow conditions," *Ann. Biomed. Eng.*, vol. 28, pp. 1281–1299, 2000.

[3] J. Wan, B. Steele, S. A. Spicer, S. Strohband, G. R. Feijóo, T. J. R. Hughes, and C. A. Taylor, "A one-dimensional finite element method for simulation based medical planning for cardiovascular disease," *Comput. Meth. Biomech. Biomed. Emg.*, vol. 5, no. 3, pp. 195–206, 2002.

[4] S. J. Sherwin, L. Formaggia, J. Peirò, and V. Franke, "Computational modelling of 1D blood flow with variable mechanical properties and its application to the simulation of wave propagation in the human arterial system," *Int. J. Numerical Meth. Fluids*, vol. 43, no. 6–7, pp. 673–700, 2003.

[5] S. Canic, "Blood flow through compliant vessels after endovascular repair: Wall deformations induced by the discontinuous wall properties," *Computing Visualization Sci.*, vol. 4, no. 3, pp. 147–155, 2002, Springer-Verlag.

[6] J. S. Yadav, G. S. Roubin, S. Iyer, J. Vitek, P. King, and W. D. Jordan, "Elective stenting of the extracranial carotid arteries," *Circulation*, vol. 95, no. 3, pp. 76–81, 1997.

[7] M. H. Wholey, M. Wholey, P. Bergeron, E. B. Diethrich, M. Henry, J. C. Laborde, K. Mathias, S. Myla, G. S. Roubin, F. Shawl, J. G. Theron, J. S. Yadav, G. Dorros, J. Guimaraens, R. Higashida, V. Kumar, M. Leon, M. Lim, H. Londero, J. Mesa, S. Ramee, A. Rodriguez, K. Rosenfield, G. Teitelbaum, and C. Vozzi, "Current global status of carotid artery stent placement," *Catheterization Cardiovasc. Diagnosis*, vol. 44, no. 1, pp. 1–6, 1998.

[8] M. S. Olufsen, "Modeling the arterial system with reference to an anaesthesia simulator," Ph.D. thesis, Roskilde Univ., Roskilde, Denmark, 1998.

[9] D. W. Holdsworth, C. J. D. Norley, R. Frayne, D. A. Steinman, and B. K. Rutt, "Characterization of common carotid artery blood-flow waveforms in normal human subjects," *Physiological Meas.*, vol. 20, pp. 219–240, 1999.

[10] J. J. Wang and K. H. Parker, "Wave propagation in a model of the arterial circulation," *J. Biomech.*, vol. 37, pp. 457–470, 2004.

[11] V. B. Kolachalama, N. W. Bressloff, P. B. Nair, and C. P. Shearman, "A parametric study of the hemodynamic behavior in a one dimensional systemic elastic artery: Application to stent design," presented at the 12th Int. Conf. Biomedical Engineering, Singapore, 2005.

[12] R. Hicks and P. Henne, "Wing design by numerical optimization," *J. Aircraft*, vol. 15, no. 7, pp. 407–413, 1978.

[13] M. D. McKay, W. J. Conover, and R. J. Beckman, "A comparison of three methods for selecting values of input variables in the analysis of output from a computer code," *Technometrics*, vol. 21, pp. 239–245, 1979.

[14] V. B. Kolachalama, "Predictive haemodynamics of the human carotid artery," Ph.D. thesis, Univ. Southampton, Southampton, U.K., 2006.

[15] J. S. Milner, J. A. Moore, B. K. Rutt, and D. A. Steinman, "Hemodynamics of human carotid artery bifurcations: Computational studies with models constructed with magnetic resonance imaging of normal subjects," *J. Vasc. Surg.*, vol. 28, pp. 143–156, 1998.

[16] I. Marshall, S. Zhao, P. Papathanasopoulou, P. Hoskins, and X. Y. Xu, "MRI and CFD studies of pulsatile flow in healthy and stenosed carotid bifurcation models," *J. Biomech.*, vol. 37, pp. 679–687, 2004.

[17] P. M. Rothwell and C. P. Warlow, for the European Carotid Surgery Trialists' Collaborative Group, "Prediction of benefit from carotid endarterectomy in individual patients: A risk-modelling study," *Lancet*, vol. 353, pp. 2105–2110, 1999.

[18] M. Schillinger, M. Haumer, S. Schillinger, R. Ahmadi, and E. Minar, "Risk stratification for subclavian artery angioplasty: Is there an increased rate of restenosis after stent implantation?," *Journal of Endovascular Therapy*, vol. 8, pp. 550–557, 2001.

[19] L. Formaggia, F. Nobile, A. Quarteroni, and A. Veneziani, "Multiscale modeling of the circulatory system: A preliminary analysis," *Computing and Visualization in Science*, vol. 2, pp. 75–84, 1999.

Author photographs and biographies not available at the time of publication.